



**HAL**  
open science

## Geologically-rapid aqueous mineral alteration at subfreezing temperatures in icy worlds

Amber Zandanel, Roland Hellmann, Laurent Truche, Vladimir Roddatis,  
Michel Mermoux, Gaël Choblet, Gabriel Tobie

► **To cite this version:**

Amber Zandanel, Roland Hellmann, Laurent Truche, Vladimir Roddatis, Michel Mermoux, et al..  
Geologically-rapid aqueous mineral alteration at subfreezing temperatures in icy worlds. *Nature Astronomy*, 2022, 10.1038/s41550-022-01613-2 . hal-03795029

**HAL Id: hal-03795029**

**<https://hal.science/hal-03795029>**

Submitted on 3 Oct 2022

**HAL** is a multi-disciplinary open access archive for the deposit and dissemination of scientific research documents, whether they are published or not. The documents may come from teaching and research institutions in France or abroad, or from public or private research centers.

L'archive ouverte pluridisciplinaire **HAL**, est destinée au dépôt et à la diffusion de documents scientifiques de niveau recherche, publiés ou non, émanant des établissements d'enseignement et de recherche français ou étrangers, des laboratoires publics ou privés.

1 **Geologically-rapid aqueous mineral alteration at subfreezing temperatures in icy worlds**

2 **Amber Zandanel<sup>1\*</sup>, Roland Hellmann<sup>1</sup>, Laurent Truche<sup>1</sup>, Vladimir Roddatis<sup>2</sup>, Michel**

3 **Mermoux<sup>3</sup>, Gaël Choblet<sup>4</sup>, Gabriel Tobie<sup>4</sup>**

4 <sup>1</sup> Université Grenoble Alpes, CNRS, ISTerre, F-38058 Grenoble Cedex 9, France

5

6 <sup>2</sup> GFZ German Research Centre for Geosciences, Telegrafenberg, D-14473 Potsdam, Germany

7 <sup>3</sup> Université Grenoble Alpes, Univ. Savoie Mont Blanc, CNRS, Grenoble INP, LEPMI, 38000

8 Grenoble, France

9 <sup>4</sup> Laboratoire de Planétologie et Géodynamique, UMR 6112, CNRS, Université de Nantes, 2  
10 chemin de la Houssinière, 44300 Nantes, France

11 \*azandanel@gmail.com

12

13 **The most active icy worlds like Europa or Enceladus are predicted to host extensive**  
14 **aqueous alteration driven by water-rock interactions at elevated temperatures<sup>1-3</sup>. On the**  
15 **other hand, it is assumed that such alteration is kinetically inhibited at the sub-zero**  
16 **temperatures of other icy worlds, such as the mid-sized moons of Saturn and Uranus or**  
17 **Trans-Neptunian Objects<sup>1,4</sup>. Here we perform aqueous alterations experiments on a**  
18 **chondrite-analogue material (olivine) and find that chemical alteration processes are**  
19 **still efficient at temperatures as low as -20 °C, as the presence of an unfrozen water film**  
20 **still allows olivine to dissolve in partially frozen alkaline solutions. We infer that**  
21 **aqueous alteration may be enhanced by salts and ammonia present in icy worlds, and**  
22 **therefore remains a geologically rapid process even at sub-zero temperatures. Our**  
23 **results imply that most icy bodies exceeding 400-500 km in diameter will be completely**  
24 **altered to hydrous secondary minerals early in their evolutionary histories.**

25 Models of icy worlds evolution often anticipate the release of heat and chemical energy  
26 through aqueous alteration or serpentinization of primary chondritic minerals when in contact  
27 with fully melted water<sup>4-6</sup>. One fundamental question is whether bulk liquid water is a  
28 necessary prerequisite to these processes, or can water-rock interactions still occur below the  
29 freezing point in icy bodies? To address this, we determined the rates and mechanism of  
30 olivine dissolution in alkaline solutions at -20, 4, and 22 °C from dissolution experiments that  
31 lasted up to 442 days. The range of temperatures chosen corresponds to those that can be  
32 achieved in mid- to large-sized icy worlds from radiogenic sources alone, in the absence of  
33 extra heat due to tidal friction<sup>4,5,7</sup>. Most icy worlds with diameters exceeding 400-500 km  
34 cross this temperature threshold when their cores, comprised of ice and rock, undergo an  
35 initial heating period. Three different solution chemistries were used at each temperature to  
36 analyse the effect of NH<sub>3</sub> concentration (0, 0.8, 8.0 mass % - hereafter %) and pH in an  
37 alkaline, dilute saline solution (H<sub>2</sub>O-NaCl-KCl-NaHCO<sub>3</sub>), such as is thought to evolve in

38 solutions interacting with a chondritic rock matrix<sup>8,9</sup> and corroborated by analyses of vapour  
39 and grains emitted in Enceladus' plumes<sup>2</sup>. At -20 °C, some unfrozen solution existed in all  
40 experiments as the NaCl-KCl-NaHCO<sub>3</sub>-H<sub>2</sub>O system has a eutectic temperature (solidus) of -  
41 24 °C<sup>10</sup>, while the H<sub>2</sub>O-NH<sub>3</sub> system has a eutectic temperature of -96 °C<sup>11</sup> (Supplementary  
42 Information 4.1-4.2 and Supplementary Fig. 5). The amount of solution that remains unfrozen  
43 increases with increasing NH<sub>3</sub> content (Table 1). At experimental conditions pure water ice  
44 formed during freezing<sup>10,11</sup>.

45 Optical microscope images of partially frozen 0.0, 0.8 and 8.0% NH<sub>3</sub> solutions illustrate  
46 decreasing crystallinity and increasing porosity in the ice phase caused by increasing NH<sub>3</sub>  
47 content (Fig. 1a-c). Visual evidence of an unfrozen solution film at the olivine-ice interface  
48 was obtained by imaging melt propagation from the ice-olivine boundary in a frozen sample  
49 allowed to equilibrate to bench temperature (Fig. 1d), and an in-situ investigation of olivine  
50 grains in frozen solutions (Fig. 1e). To identify solutes concentrated in the unfrozen film at  
51 the olivine interface, Raman analyses were performed at -20 °C on an amalgam of olivine  
52 grains, ice, and unfrozen solutions using a temperature-controlled stage. Raman spectra,  
53 which probed the transition from ice to interfacial liquid water, show that the shape of the  
54 broad symmetric and asymmetric OH-stretching band of water at 2900–3800 cm<sup>-1</sup> evolves  
55 when approaching the olivine surface, characterized by an upward shift of the entire band and  
56 a clear decrease in the intensity of the region <3325 cm<sup>-1</sup> that corresponds to symmetric OH-  
57 stretching (Supplementary Figs. 3, 4). In addition, the intensities of NH<sub>3</sub> and CO<sub>3</sub><sup>2-</sup> peaks  
58 positively correlate with the broadening and intensity decrease of the spectral component  
59 centred at 3138 cm<sup>-1</sup>, which is clearly defined in ice. These observations corroborate the  
60 accumulation of NH<sub>3</sub> and CO<sub>3</sub><sup>2-</sup> in the unfrozen solution enveloping the olivine grains.

61 Increasing silica and magnesium concentrations with time indicate that olivine dissolution  
62 occurred continuously at all experimental conditions (Fig. 2a-c). We derived separate

63 apparent olivine dissolution rates ( $\text{mol m}^{-2} \text{s}^{-1}$ ) from aqueous [Si] and [Mg] (denoted  $r_{\text{Si}}$  and  
64  $r_{\text{Mg}}$ ), and split them into two regimes based on reaction progress: initial rates (furthest from  
65 equilibrium,  $\Delta G_{\text{diss}} \ll 0$ ; 0-14d) and long-term rates (closer to equilibrium,  $\Delta G_{\text{diss}} < 0$ ; 167d).  
66 These rates are “apparent” as any sequestration of Mg or Si in secondary phases decreases  
67 their respective aqueous concentrations, resulting in lower calculated olivine dissolution rates.

68 The initial apparent dissolution rates  $r_{\text{Si}}$  and  $r_{\text{Mg}}$  are relatively clustered at  $-20\text{ }^{\circ}\text{C}$ , indicating  
69 nearly stoichiometric alteration (Fig. 2d). With increasing temperature  $r_{\text{Si}}$  and  $r_{\text{Mg}}$  increasingly  
70 diverge from one another, with  $r_{\text{Mg}}$  generally lower than  $r_{\text{Si}}$ . The majority of the initial  $r_{\text{Si}}$  and  
71  $r_{\text{Mg}}$  also show a modest increase with increasing temperature from  $-20$  to  $4\text{ }^{\circ}\text{C}$ , whereas from  
72  $4$  to  $22\text{ }^{\circ}\text{C}$ , two of the  $r_{\text{Si}}$  rates and all of the  $r_{\text{Mg}}$  show no meaningful dependence on  
73 temperature (Methods). Previous experimental studies that characterized olivine dissolution at  
74 below  $0\text{ }^{\circ}\text{C}$  focused on highly acidic solutions<sup>14,15</sup>, and rapid dissolution rates were ascribed to  
75 an acid concentration effect in an unfrozen fluid phase<sup>15</sup>. However, as the mechanism of  
76 olivine dissolution is thought to change from acid to alkaline conditions<sup>12</sup>, acid-pH olivine  
77 dissolution rates cannot be directly applied to alkaline conditions. The overall trends from our  
78 experiments show a weak inverse relation between pH and dissolution rates in the alkaline pH  
79 range, consistent with published alkaline olivine dissolution rates at ambient temperatures<sup>12,13</sup>.

80 In contrast, the individual  $r_{\text{Si}}$  show a positive correlation with ammonia concentration at a  
81 given pH: despite having identical pH at  $22\text{ }^{\circ}\text{C}$ ,  $r_{\text{Si}}$  is higher in all experiments with  $0.8\%$   $\text{NH}_3$   
82 compared to  $0\%$   $\text{NH}_3$  (Fig. 2d).

83 Long-term apparent rates ( $ltr_{\text{Si}}$  and  $ltr_{\text{Mg}}$ ) decrease with temperature from  $-22$  to  $4\text{ }^{\circ}\text{C}$  but are  
84 roughly equivalent at  $4$  and  $22\text{ }^{\circ}\text{C}$  (Fig. 2e). All rates appear to approach steady state at 167d,  
85 while the experiments that lasted 442d ( $0.8\%$   $\text{NH}_3$ ) show a curious increase in concentrations  
86 (Fig. 2a-c; 167-443d), correlating to a slight transient increase in rates. In terms of  
87 stoichiometry,  $ltr_{\text{Mg}} > ltr_{\text{Si}}$  at  $-20\text{ }^{\circ}\text{C}$ , but at  $4$  and  $22\text{ }^{\circ}\text{C}$   $ltr_{\text{Si}}$  and  $ltr_{\text{Mg}}$  generally come close to

88 converging ( $ltr_{Mg} \geq ltr_{Si}$ ). Long-term  $ltr_{Si}$  are relatively constant with increasing pH at 4 and 22  
89 °C, with only a weak positive relation recorded at -20 °C.

90 All of the experiments displayed varying degrees of non-stoichiometric olivine alteration  
91 behaviour, with  $r_{Si} > r_{Mg}$  or  $ltr_{Mg} \geq ltr_{Si}$ . The increasing degree of non-stoichiometry in  $r_{Si}$  and  
92  $r_{Mg}$  with temperature, as well as very low activation energies, are evidence that released Mg  
93 and Si were being pulled out of solution and incorporated into secondary authigenic phases  
94 (Methods). Finally, the non-stoichiometric long-term rates at -20 °C indicate potential  
95 secondary phase formation occurring even in the partially frozen experiments (Fig. 2e). Both  
96 the initial ( $r_{Si}$ ,  $r_{Mg}$ ) and long-term ( $ltr_{Si}$ ,  $ltr_{Mg}$ ) apparent rates calculated at 4 and 22 °C cannot,  
97 therefore, be considered equivalent to far-from-equilibrium olivine dissolution rates  
98 (Supplementary Information 2.2). Our apparent rates rather describe an overall alteration  
99 process occurring at conditions much closer to equilibrium, and thus more similar to the rates  
100 expected on icy bodies.

101 Observation of olivine grains at the micron scale (SEM) revealed no visible alteration features  
102 at the olivine surface (Fig. 3a). However, at the nanoscale, evidence of the formation of a non-  
103 crystalline (amorphous) secondary phase at the olivine surface is apparent. In high-resolution  
104 iDPC-STEM images (Fig. 3b), the olivine lattice fringes abruptly terminate at a surface  
105 altered layer (SAL), here an irregular <1 nm-wide band of material without an ordered  
106 structure (Fig. 3b). The long-term dissolution rates ( $ltr_{Mg} > ltr_{Si}$ ; Fig. 2e) suggest possible  
107 preferential sequestration of Si in this SAL. From the aqueous chemistry we further calculated  
108 the theoretical thicknesses of SALs (Supplementary Information 2.3); typical values were  
109 found to be <10 Å, consistent with our observations.

110 We propose that the mechanism for this alteration is the unfrozen film of solution at the ice-  
111 olivine interface, which may also be enriched in ammonia due to its exclusion from the ice

112 phase. During melting/refreezing, the chemical potential at the solution-mineral interface  
113 causes an interfacial liquid film to form around mineral grains that persists below the partial  
114 freezing point (liquidus) and even the total freezing point (solidus) of the bulk solution<sup>16,17</sup>.  
115 The olivine alteration observed in our experiments validates a proposed mechanism for  
116 aqueous mineral alteration signatures previously observed in chondrites<sup>18</sup> and in extreme  
117 environments in Antarctica<sup>19</sup>. Alteration at sub-zero temperatures at alkaline conditions has  
118 far-reaching implications for interpreting the present day mineralogy of the rocky cores of icy  
119 worlds, as exothermic mineral weathering is predicted at any temperature where this liquid  
120 film forms, further enhanced by antifreeze agents (salts, NH<sub>3</sub>) that increase the width of this  
121 film and thus the liquid water-rock ratio<sup>17</sup>.

122 Based on long-term rates observed at -20 °C in our experiments (Fig. 2e), we assessed that the  
123 heating rate generated by olivine dissolution (up to  $2.3 \times 10^{-8}$  to  $4.6 \times 10^{-7}$  W kg<sup>-1</sup>, Methods) is  
124 comparable to that generated by short-lived radioactive nuclides (e.g., <sup>26</sup>Al), and may provide  
125 a heat pulse for periods of tens to hundreds of millions years after accretion<sup>4,5</sup>. We posit that  
126 during progressive radiogenic heating of initially frozen interiors, aqueous alteration should  
127 commence at least when the first aqueous melts appear in the deepest regions (as low as -96  
128 °C, depending on volatile and salt contents). Melting is expected to propagate throughout the  
129 entire core at timescales ranging between a few tens to hundreds of millions of years,  
130 depending on the body size and available heat sources<sup>4,5</sup>. Given the relatively fast apparent  
131 dissolution rates observed in our experiments, we predict that alteration will be controlled by  
132 the outward propagation rate of melt front, resulting in alteration of most of the silicate core.  
133 This process likely controlled the early evolution of most icy worlds, including Ceres,  
134 Saturn's and Uranus' mid-sized moons (Mimas, Enceladus, Dione, Ariel, Oberon, Titania)<sup>1</sup>,  
135 and TNOs with diameters >500 km<sup>7</sup>. Low core densities of Ceres (2400-2900 kg m<sup>-3</sup>)<sup>20</sup>,  
136 Enceladus (2400-2500 kg m<sup>-3</sup>)<sup>21</sup>, and Dione (2400-2500 kg m<sup>-3</sup>)<sup>22</sup> corroborate the hypothesis

137 that the rocky cores of these worlds are largely composed of altered hydrated minerals.

138 This initial period of geologically-rapid chemical alteration of primary ultramafic minerals  
139 (Fe and Mg-rich silicates, such as olivine, pyroxene), associated with H<sub>2</sub> production<sup>23</sup>, may  
140 have produced potentially habitable rock-water-hosted environments even at relatively low  
141 temperatures. After this first widespread alteration stage, active alteration of primary minerals  
142 was likely limited to only a few bodies in the Solar system where fresh minerals are  
143 continuously brought in contact with water, notably on Earth at mid-oceanic ridges, but also  
144 possibly on Europa's seafloor<sup>24</sup>.

145 Even though our data support a new scenario where serpentinization reactions no longer play  
146 a major role on icy moons, this does not imply that these bodies are geochemically quiescent.  
147 For instance, chemical data from Enceladus should now be viewed within the framework of  
148 water-rock interactions other than serpentinization of primary minerals: our results suggest  
149 that the low yields of H<sub>2</sub> may be explained by oxidization of Fe(II) in secondary minerals  
150 such as serpentine, siderite and Fe-bearing brucite<sup>2</sup>. Alternatively, other processes may be  
151 ongoing, such as hydrothermal pyrolysis of primordial organics or biotic methanogenesis, as  
152 recently invoked to explain the rough equivalence of H<sub>2</sub> and CH<sub>4</sub> in the plumes of  
153 Enceladus<sup>25</sup>.

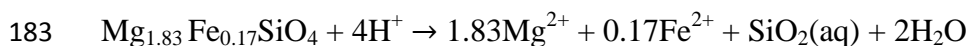
154 More generally, our results imply that secondary altered minerals should be ubiquitous in the  
155 interiors of icy moons and parent bodies of carbonaceous chondrites. Altered mineral  
156 assemblages in the samples retrieved by Hayabusa2 and OSIRIS-Rex, including detailed  
157 investigations of SALs, will provide crucial information about past aqueous environments in  
158 the parent bodies of Ryugu and Bennu<sup>26</sup>. Similar to what was observed on Ceres with Dawn<sup>27</sup>,  
159 identification of alteration products by the upcoming observation campaigns using the James  
160 Webb Spatial Telescope and the Lucy mission to the Trojan asteroids may confirm the  
161 ubiquity of aqueous processes, even in distant icy worlds.



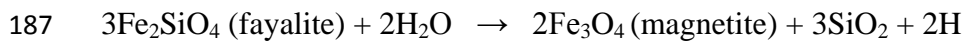
## 162 **Methods**

163 Batch reactor experiments were carried out at -20, 4 and 22 °C for variable periods of time  
164 ranging from 41 to 442 days. Three experimental series were carried out at each temperature,  
165 with each series being comprised of numerous Nalgene vials, each containing 0.3 g of San  
166 Carlos olivine grains ( $\text{Mg}_{1.83}\text{Fe}_{0.17}\text{SiO}_4$ ) sieved to 0.05-0.125 mm size range, and 30 mL of  
167 saline fluid containing either 0.0, 0.8, or 8.0 mass %  $\text{NH}_3$  (0.0 %  $\text{NH}_3$  solution prepared with  
168 NaOH). The starting  $\text{pH}_{(25\text{ }^\circ\text{C})}$  values of the solutions were 10.8, 10.8, and 12.2, respectively.  
169 Vials were then sequentially removed from the experiment at designated times and sampled  
170 post-mortem (fluid chemistry shown in Fig. 2a-c). All experiments were carried out at  
171 ambient pressure (1 bar). Pressure is not a crucial variable as pressures in mid-sized icy  
172 bodies that maintain relevantly low temperatures will have correspondingly low pressures (for  
173 example, <400 bar maximum in a core the size of Enceladus<sup>28</sup>), at which pressure is not  
174 known to have significant effects on olivine alteration processes<sup>29</sup>. Mg-rich olivine (forsterite)  
175 was selected for these experiments as a common and dominant primary mineral found in the  
176 chondrites<sup>30,31</sup> that are thought to make up icy worlds<sup>2,3,9</sup>. In addition, olivine is of specific  
177 interest as a primary mafic mineral that drives serpentinization reactions and the production of  
178  $\text{H}_2$ <sup>1,9</sup>. The overall composition, ratios of salts, and  $\text{NH}_3$  concentrations of the solution were  
179 chosen to bracket the chemistry of solutions predicted to evolve from chondrite-fluid  
180 interactions<sup>32,33</sup>. Additional information on the experimental approach is discussed in  
181 Supplementary Information 1.1-1.3.

182 The olivine dissolution reaction at our experimental conditions can be represented by:



184 This reaction is related but distinct from a serpentinization reaction. Based on the two olivine  
185 solid solution end members, serpentinization reactions can be expressed as follows:



188 There is currently no consensus whether a lower temperature bound for serpentinization  
189 exists. Studies postulate these reactions continue down to  $10^\circ\text{C}$ <sup>23</sup>, although recent field  
190 studies of ophiolite weathering suggest that observed  $\text{H}_2$  and  $\text{CH}_4$  production at low  
191 temperatures are attributable to later stages of water-rock interaction with secondary, rather  
192 than primary, minerals<sup>34</sup>. While our experiments were limited in time (max. 442 days), we can  
193 speculate that over significantly longer time periods the amorphous SALs that formed on the  
194 olivine grains could serve as a matrix for the in situ nucleation of poorly crystalline proto-  
195 serpentine phase(s), especially in light of the chemical oversaturation with respect to  
196 serpentine minerals in many of our experiments (Supplementary Information 4.3 and 4.4).  
197 Such proto-serpentine have been observed as a precursor step in serpentinization reactions<sup>35</sup>.  
198 The major aqueous cations were analysed by inductively coupled plasma atomic emission  
199 spectroscopy (ICP-AES). Apparent dissolution rates were calculated from the aqueous  
200 concentrations of Mg and Si: initial apparent dissolution rates ( $r_{\text{Si}}$  and  $r_{\text{Mg}}$ ) were calculated  
201 based on linear regressions of the concentration data from  $t = 0$  to 14 d; long-term apparent  
202 rates ( $ltr_{\text{Si}}$  and  $ltr_{\text{Mg}}$ ) were derived from the  $dc/dt$  slope of the aqueous concentration data at  
203 167d (Supplementary Information 2.1 and Supplementary Fig. 1). Rates based on aqueous Fe  
204 concentrations were not calculated as this element was generally below analytical detection  
205 limits (Supplementary Information 6). As a reminder concerning mineral dissolution kinetics,  
206 the concentrations of Si and Mg at a given time in a reactor reflect the dynamic relation  
207 between two fundamental processes: their release from the olivine structure and their  
208 subsequent incorporation into secondary authigenic phases (both crystalline and amorphous-  
209 see details in Supplementary Information 2.3). The degree of incorporation into authigenic  
210 phases is both element-specific and depends on temperature and other physico-chemical

211 parameters. Because the formation of authigenic phases decreases the aqueous concentrations  
212 of the element(s) used to calculate the thermal activation energy  $E_a$  (Si, Mg), this decreases  
213 the slope of the  $\ln k$  vs  $1/T$  relation used to calculate  $E_a$  (Supplementary Fig. 2). The  
214 attenuated dependency of  $r_{\text{Si}}$  on temperature that we measured is therefore reflected in the  
215 thermal activation energies ( $E_a = 12\text{-}19 \text{ kJ mol}^{-1}$ ) determined from the initial apparent rates of  
216 olivine dissolution at  $T = -20, 4$  and  $22 \text{ }^\circ\text{C}$ . These values are lower than the average value of  
217  $\sim 63 \text{ kJ mol}^{-1}$  from compiled rate data<sup>13</sup>. Further details on the calculation of  $E_a$  are given in  
218 Supplementary Information 2.1-2.2; derived rates are listed in Supplementary Table 1.

219 The heating rate of olivine dissolution was calculated from the average  $ltr_{\text{Si}}$  ( $1.2 \times 10^{-13} \text{ mol m}^{-2}$   
220  $\text{s}^{-1}$ ) of all experiments at  $-20 \text{ }^\circ\text{C}$  (Fig. 2), with a  $\Delta H$  of  $203 \text{ kJ mol}^{-1}$  released during  
221 dissolution<sup>36</sup>. Heating rates can then be scaled to surface areas to calculate heating rates for a  
222 mass unit of olivine having grain sizes different from those used in our experiments. The  
223 range of heating rates presented above were calculated using geometric surface areas for  
224 olivine grain sizes common to chondrites (0.05-1 mm radius, with surface areas of 18.5-0.923  
225  $\text{m}^2 \text{ kg}^{-1}$ )<sup>31</sup>.

226 To image olivine in partially frozen aqueous solutions we used optical microscopy (plain and  
227 polarized light) to observe the nature of the olivine-ice interface and the porosity of the  
228 enveloping adjacent ice. The microscopy work was done in a cold room at  $-8 \text{ }^\circ\text{C}$ . The physical  
229 process of fluid melting at the olivine grain-ice interface was also studied with a mixture of  
230 unreacted olivine grains (crushed, sieved and cleaned identically to olivine used in the  
231 experiments, but not included in the experiments) and deionized water that was frozen with  
232 liquid  $\text{N}_2$  (77 K). The frozen mixture was then observed under an optical microscope at  
233 ambient temperature so that we could record sequential images of the liquid solution front  
234 propagating away from the olivine grain as the temperature gradually rose. Raman analyses of  
235 olivine, ice, and unfrozen fluid were performed at the olivine-ice interface using a Renishaw®

236 InVia confocal Raman microscope. Samples (unreacted olivine grains and solution) were  
237 placed in a quartz cell in a Linkam® THMS 600 heating/freezing stage and maintained at -20  
238 °C during analyses. Measurements were performed at 532 nm using a 50x-long working  
239 distance objective.

240 Post-reaction olivine grains were imaged by field emission scanning electron microscopy  
241 (FEG SEM, Zeiss Ultra 55, CMTC, Univ. Grenoble Alpes) at 20 kV to characterize the  
242 presence and degree of surface coverage of potential secondary phases (crystalline and/or  
243 amorphous). Reacted olivine grains (10-15 grains total) originating from experiments in each  
244 solution were used for EDX spot analyses. For all analyses, conchoidal fracture surfaces were  
245 carefully selected to avoid any pre-existing alteration features on unaltered grains  
246 (Supplementary Information 5.1). SEM images and EDX analyses of grain surfaces from all  
247 grain sets did not reveal any dissolution features, such as etch pits, or surface precipitates.  
248 EDX spot analyses of post reaction surfaces were not distinguishable from those measured on  
249 unreacted olivine (in both cases, the nominal compositional stoichiometry of San Carlos  
250 olivine was confirmed). Some remaining surface fines (micrometre-sized grain fragments  
251 created during comminution) seem to have been present on both unreacted and reacted grains  
252 (e.g., Fig. 3a).

253 Detailed high-resolution analyses by transmission electron microscopy (TEM) were centred  
254 on three altered olivine grains subjected to 442 d of reaction at -20 °C in a 0.8 % NH<sub>3</sub> saline  
255 solution, as this experiment was subject to the longest reaction times. Here, the purpose was  
256 to examine structural and chemical changes to the near surface region, which included the  
257 formation of secondary phases, in the form of mineral (crystalline) phases or amorphous  
258 phases. We examined these samples in cross section with electron transparent foils prepared  
259 by focused ion beam (FIB) milling (Supplemental Information 5.2) using standard preparation  
260 techniques<sup>37</sup>. These observations were then compared to samples from unreacted olivine

261 grains prepared in an identical manner (Supplementary Figs. 6-9). TEM analyses were  
262 performed using a state-of-the-art Thermo Fisher Scientific Themis Z 3.1 operated at 300 kV,  
263 and a Tecnai F20 operated at 200 kV, both housed at the GFZ-PISA facility, Potsdam. We  
264 used standard bright and dark field (BF, DF), scanning TEM-high angle annular dark field  
265 (STEM-HAADF), and integrated Differential Phase Contrast STEM (iDPC-STEM) imaging  
266 techniques<sup>38,39</sup>, while high resolution chemical analyses were carried out with EELS spectral  
267 imaging in STEM mode (Supplemental Information 5.3). The chemical composition of the  
268 very thin amorphous SALs (Fig. 3b) could not be measured because of their sensitivity to the  
269 electron beam. It is interesting to note that the extreme thinness of the SALs indicates that  
270 they would not have acted as a diffusion barrier to the release of Si and Mg from the olivine  
271 structure. On the other hand, diffusion limitations can potentially occur for much thicker (up  
272 to tens of nm) SALs<sup>40</sup>.

273 Further details concerning methods, materials, instrumental parameters and techniques can be  
274 found in the Supplementary Information.

275 **Data availability:** Additional data and complete analysed fluid chemistries are included in  
276 Supplementary Information and Supplementary Tables 2-11.

277 **Corresponding author:** correspondence to A. Zandanel.

278 **Acknowledgments:** This study acknowledges the financial support from the French Agence  
279 Nationale de Recherche, project ANR OASIS (grant N° ANR-16-CE31-0023-01). We thank  
280 Y. Marrocchi for the raw San Carlos olivine and Selfrag AG (Kerzers, Switzerland) for the  
281 high voltage pulsed power fragmentation of the original San Carlos olivine sample. The use of  
282 equipment in the “Potsdam Imaging and Spectral Analysis Facility” (PISA) is acknowledged.  
283 The authors especially thank the European Regional Development Fund and the State of  
284 Brandenburg for the Themis Z TEM (part of PISA). Chemical analyses by ICP-AES and BET

285 surface area measurements were performed at the geochemistry-mineralogy platform of  
286 ISTERre (UGA, Grenoble, France), partially funded by a grant from Labex OSUG@2020. We  
287 also thank A. Schreiber (GFZ) for her help in developing the FIB technique used, N. Findling  
288 (ISTERre) for assistance with the sub-zero alteration experiments.

289 **Author contributions:** L.T. designed the project. A.Z. performed the experiments, ICP-AES  
290 analyses, and geochemical modelling. R.H. evaluated the kinetic behaviour of olivine  
291 dissolution and interpreted TEM results with V.R. FIB and TEM work was carried out by  
292 V.R. Raman analyses were performed and interpreted by M.M. The manuscript was written  
293 by A.Z., R.H., G.T., and L.T., with contributions from all co-authors. All co-authors  
294 contributed to the discussion and interpretation of the data.

295 **Competing interests:** The authors declare no competing interests.

296

297 **Tables**298 **Table 1**

Table 1: Physiochemical parameters									
Solution	NaOH (0 % NH <sub>3</sub> )			0.8 mass % NH <sub>3</sub>			8.0 mass % NH <sub>3</sub>		
Temp (°C)	22	4	-20	22	4	-20	22	4	-20
Fluid : Ice	30 : 0	30 : 0	1 : 29	30 : 0	30 : 0	2 : 28	30 : 0	30 : 0	13 : 17
Fluid : Rock	100 : 1	100 : 1	2 : 1	100 : 1	100 : 1	6 : 1	100 : 1	100 : 1	42 : 1
Ionic strength	0.1	0.1	5.1	0.11	0.11	1.89	0.09	0.09	0.22
Molal NH <sub>3</sub>	0	0	0	0.5	0.5	6.7	4.7	4.7	9.6
In-situ pH	10.8	11.1	11.5	10.8	11.5	11.9	12.1	12.8	13.7
Duration (days)	167	167	41	442	442	442	41	167	167

299 **Table 1: Initial physiochemical characteristics of each experiment.**

300 “Fluid : Ice” indicates the mass ratio of unfrozen solution remaining to the moles of ice formed in each  
 301 reactor. “Fluid : rock” indicates the mass ratio of unfrozen solution in each reactor to olivine, not  
 302 including the mass of the unfrozen solution films at the mineral grain surface. Ionic strength, molal  
 303 NH<sub>3</sub>, and in-situ pH refer to properties of the in-situ unfrozen solution. In-situ pH was calculated with  
 304 the code FREZCHEM<sup>10</sup> from the measured bench temperature of each solution, and increases due to  
 305 temperature effects at 4 °C, and due to temperature effect and solute exclusion from the ice phase at -  
 306 20 °C. Note that at 22 °C the pH of the 0.8 % NH<sub>3</sub> solution is identical to the 0 % solution, but is  
 307 lower than that of the 0 % solution at 4 °C and -20 °C.

308

309 **Display elements legends (Figures submitted separately)**310 **Fig. 1: Characterization of the ice, unfrozen solution, and ice-olivine interface.**

311 **a-c:** Images taken by an optical microscope in polarized transmission mode of the three solutions used  
 312 in this study at -8°C: **a.** 0.0 % NH<sub>3</sub>. **b.** 0.8 % NH<sub>3</sub>. **c.** 8.0 % NH<sub>3</sub>. Increased birefringence (highest  
 313 birefringence visible as vivid blue) of the ice phase indicates increased crystallinity (Supplementary  
 314 Information 3.1). Crystallinity of the ice phase increases with decreasing NH<sub>3</sub> content. **d.** Image of  
 315 olivine crystals and deionized water flash-frozen with liquid N<sub>2</sub> and rapidly imaged under a  
 316 microscope at room temperature to capture outward propagation of melt. **e.** Representative image of  
 317 olivine in frozen solution taken with non-polarized light. **f.** Annotated compilation of three Raman  
 318 spectra collected at -20 °C with spectral resolution 0.3-1 cm<sup>-1</sup>. Two insets show the peaks unique to the  
 319 spectra collected at the ice-olivine boundary. The gradual phase transitions recorded in the interfacial  
 320 region are an instrumental artifact, the true gradients are much sharper (Supplementary Information  
 321 3.2).

322

323

324 **Fig. 2: Measured [Si] and [Mg] concentrations over time and calculated olivine dissolution rates**  
 325 **over temperature.**

326 **a. b. c.** Concentrations of Si (circles) and Mg (diamonds) ( $\text{mmol L}^{-1} \times 10^{-2}$ ) in the fluid for the longest  
327 running experiment sets (0.8 %  $\text{NH}_3$ ) at each experimental temperature. Concentrations at  $-20^\circ\text{C}$  (c)  
328 are for the bulk (melted) solution. Error bars indicate instrumental error. **d.** Initial (0-14 day) apparent  
329 dissolution rates  $r_{\text{Si}}$  and  $r_{\text{Mg}}$  over temperature. Divergence between values for  $r_{\text{Si}}$  and  $r_{\text{Mg}}$  in the same  
330 experiment indicates that the rates become more non-stoichiometric with increasing temperature. **e.**  
331 Long-term (167 day) dissolution rates  $ltr_{\text{Si}}$  and  $ltr_{\text{Mg}}$  with respect to temperature for all experiments  
332 (two experiments were excluded due to reactor failure: see Supplementary Information 6). Error bars  
333 show error calculated from summing standard errors of each sample used in the rate analysis and  
334 standard deviations of the replicate samples at 167 h. In all panels, where error bars are not visible,  
335 error is smaller than the symbols.

336

337

338 **Fig. 3: Solid-state analysis of an olivine grain reacted in 0.8 mass %  $\text{NH}_3$  for 442 days at  $-20^\circ\text{C}$ .**

339 **a.** SEM image of reacted olivine sample surface showing location where the FIB foil was cut (arrow).  
340 Note the lack of any obvious surface precipitates or etch pits. **b.** FIB-prepared TEM foil of the same  
341 altered sample imaged by iDPC-STEM. The interfacial region is characterized by lattice fringes of  
342 unaltered olivine and an Au layer applied before FIB preparation (post-reaction surface). The two  
343 phases are separated by a thin surface altered layer (SAL) lacking an ordered structure. The SAL  
344 delimits the position of the solvent-olivine interface when the grain was removed from solution. The  
345 colored atoms represent an atomic-scale overlay of the forsterite olivine structure.

346

347

## 348 **References**

- 349 1. Vance, S. D. & Melwani Daswani, M. Serpentinite and the search for life beyond Earth. *Philos.*  
350 *Trans. R. Soc. A* **378**, (2020).
- 351 2. Waite, J. *et al.* Cassini finds molecular hydrogen in the Enceladus plume: Evidence for  
352 hydrothermal processes. *Science* **356**, 155–159 (2017).
- 353 3. Hsu, H.-W. *et al.* Ongoing hydrothermal activities within Enceladus. *Nature* **519**, 207–210 (2015).
- 354 4. Malamud, U. & Prialnik, D. Modeling Kuiper belt objects Charon, Orcus and Salacia by means of  
355 a new equation of state for porous icy bodies. *Icarus* **246**, 21–36 (2015).
- 356 5. Malamud, U. & Prialnik, D. A 1-D evolutionary model for icy satellites, applied to Enceladus.  
357 *Icarus* **268**, 1–11 (2016).
- 358 6. Palguta, J., Schubert, G. & Travis, B. J. Fluid flow and chemical alteration in carbonaceous  
359 chondrite parent bodies. *Earth Planet. Sci. Lett.* **296**, 235–243 (2010).



- 360 7. Guilbert-Lepoutre, A., Prialnik, D. & Métayer, R. Internal structure and cryovolcanism on Trans-  
361 Neptunian objects. in *The Trans-Neptunian Solar System* 183–201 (Elsevier, 2020).
- 362 8. Ohnishi, I. & Tomeoka, K. Hydrothermal alteration experiments of enstatite: implications for  
363 aqueous alteration of carbonaceous chondrites. *Meteorit. Planet. Sci.* **42**, 49–61 (2007).
- 364 9. Sekine, Y. *et al.* High-temperature water–rock interactions and hydrothermal environments in the  
365 chondrite-like core of Enceladus. *Nat. Commun.* **6**, 8604 (2015).
- 366 10. Marion, G. M. & Kargel, J. S. *Cold aqueous planetary geochemistry with FREZCHEM: from*  
367 *modeling to the search for life at the limits.* (Springer Science & Business Media, 2007).
- 368 11. Marion, G., Kargel, J., Catling, D. & Lunine, J. Modeling ammonia–ammonium aqueous  
369 chemistries in the Solar System’s icy bodies. *Icarus* **220**, 932–946 (2012).
- 370 12. Pokrovsky, O. S. & Schott, J. Kinetics and mechanism of forsterite dissolution at 25 °C and pH  
371 from 1 to 12. *Geochim. Cosmochim. Acta* **64**, 3313–3325 (2000).
- 372 13. Rimstidt, J. D., Brantley, S. L. & Olsen, A. A. Systematic review of forsterite dissolution rate  
373 data. *Geochim. Cosmochim. Acta* **99**, 159–178 (2012).
- 374 14. Hausrath, E. & Brantley, S. L. Basalt and olivine dissolution under cold, salty, and acidic  
375 conditions: What can we learn about recent aqueous weathering on Mars? *J. Geophys. Res.*  
376 *Planets* **115**, E12001 (2010).
- 377 15. Niles, P. B., Michalski, J., Ming, D. W. & Golden, D. Elevated olivine weathering rates and  
378 sulfate formation at cryogenic temperatures on Mars. *Nat. Commun.* **8**, 998 (2017).
- 379 16. Anderson, D. M. The interface between ice and silicate surfaces. *J. Colloid Interface Sci.* **25**, 174–  
380 191 (1967).
- 381 17. Barer, S., Churaev, N., Derjaguin, B., Kiseleva, O. & Sobolev, V. Viscosity of nonfreezing thin  
382 interlayers between the surfaces of ice and quartz. *J. Colloid Interface Sci.* **74**, 173–180 (1980).
- 383 18. Rietmeijer, F. J. A model for diagenesis in proto-planetary bodies. *Nature* **313**, 293–294 (1985).
- 384 19. Dickinson, W. W. & Rosen, M. R. Antarctic permafrost: An analogue for water and diagenetic  
385 minerals on Mars. *Geology* **31**, 199–202 (2003).
- 386 20. Park, R. *et al.* A partially differentiated interior for (1) Ceres deduced from its gravity field and  
387 shape. *Nature* **537**, 515–517 (2016).

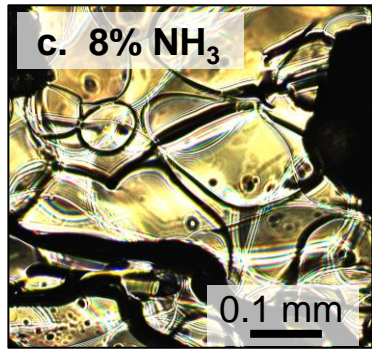
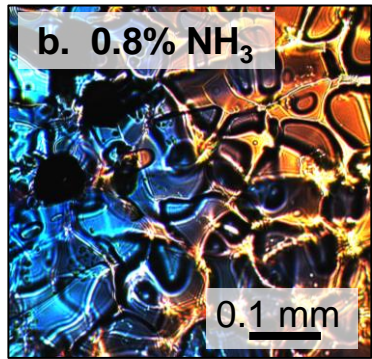
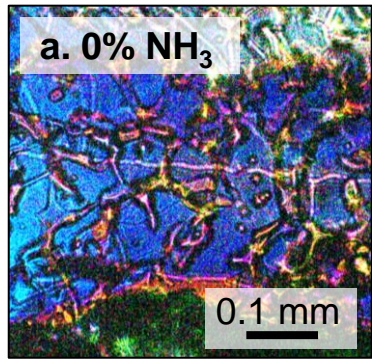
- 388 21. Iess, L. *et al.* The gravity field and interior structure of Enceladus. *Science* **344**, 78–80 (2014).
- 389 22. Zannoni, M., Hemingway, D., Casajus, L. G. & Tortora, P. The gravity field and interior structure  
390 of Dione. *Icarus* **345**, 113713 (2020).
- 391 23. Bach, W. Some compositional and kinetic controls on the bioenergetic landscapes in oceanic  
392 basement. *Front. Microbiol.* **7**, 107 (2016).
- 393 24. Běhounková, M. *et al.* Tidally Induced Magmatic Pulses on the Oceanic Floor of Jupiter’s Moon  
394 Europa. *Geophys. Res. Lett.* **48**, e2020GL090077 (2021).
- 395 25. Affholder, A., Guyot, F., Sauterey, B., Ferrière, R. & Mazevet, S. Bayesian analysis of  
396 Enceladus’s plume data to assess methanogenesis. *Nat. Astron.* 1–10 (2021).
- 397 26. Brunetto, R. & Lantz, C. Laboratory perspectives on sample returns from Hayabusa2 and OSIRIS-  
398 REx. *Nat. Astron.* **3**, 290–292 (2019).
- 399 27. Marchi, S. *et al.* An aqueously altered carbon-rich Ceres. *Nat. Astron.* **3**, 140–145 (2019).
- 400 28. Choblet, G. *et al.* Powering prolonged hydrothermal activity inside Enceladus. *Nat. Astron.* **1**, 841  
401 (2017).
- 402 29. O’Hanley, D. S. *Serpentinites: records of tectonic and petrological history.* (Oxford University  
403 Press on Demand, 1996).
- 404 30. Rubin, A. E., Trigo-Rodríguez, J. M., Huber, H. & Wasson, J. T. Progressive aqueous alteration  
405 of CM carbonaceous chondrites. *Geochim. Cosmochim. Acta* **71**, 2361–2382 (2007).
- 406 31. Rubin, A. E. Size- frequency distributions of chondrules in CO<sub>3</sub> chondrites. *Meteoritics* **24**, 179–  
407 189 (1989).
- 408 32. Zolotov, M. Y. An oceanic composition on early and today’s Enceladus. *Geophys. Res. Lett.* **34**,  
409 L23203 (2007).
- 410 33. Glein, C. R., Baross, J. A. & Waite, J. The pH of Enceladus’ ocean. *Geochim. Cosmochim. Acta*  
411 **162**, 202–219 (2015).
- 412 34. Miller, H. M. *et al.* Modern water/rock reactions in Oman hyperalkaline peridotite aquifers and  
413 implications for microbial habitability. *Geochim. Cosmochim. Acta* **179**, 217–241 (2016).

- 414 35. Lafay, R., Fernandez-Martinez, A., Montes-Hernandez, G., Auzende, A. L. & Poulain, A.  
415 Dissolution-reprecipitation and self-assembly of serpentine nanoparticles preceding chrysotile  
416 formation: Insights into the structure of proto-serpentine. *Am. Mineral.* **101**, 2666–2676 (2016).
- 417 36. Ball, J. & Nordstrom, D. *User's Manual for WATEQ4F, with Revised Thermodynamic Data Base*  
418 *and Test Cases for Calculating Speciation of Major, Trace, and Redox Elements in Natural*  
419 *Waters*. 189 (1991).
- 420 37. Schaffer, M., Schaffer, B. & Ramasse, Q. Sample preparation for atomic-resolution STEM at low  
421 voltages by FIB. *Ultramicroscopy* **114**, 62–71 (2012).
- 422 38. Lazić, I., Bosch, E. G. & Lazar, S. Phase contrast STEM for thin samples: Integrated differential  
423 phase contrast. *Ultramicroscopy* **160**, 265–280 (2016).
- 424 39. Bosch, E. G. & Lazić, I. Analysis of HR-STEM theory for thin specimen. *Ultramicroscopy* **156**,  
425 59–72 (2015).
- 426 40. Daval, D. *et al.* Influence of amorphous silica layer formation on the dissolution rate of olivine at  
427 90 °C and elevated pCO<sub>2</sub>. *Chem. Geol.* **284**, 193–209 (2011).
- 428
- 429
- 430

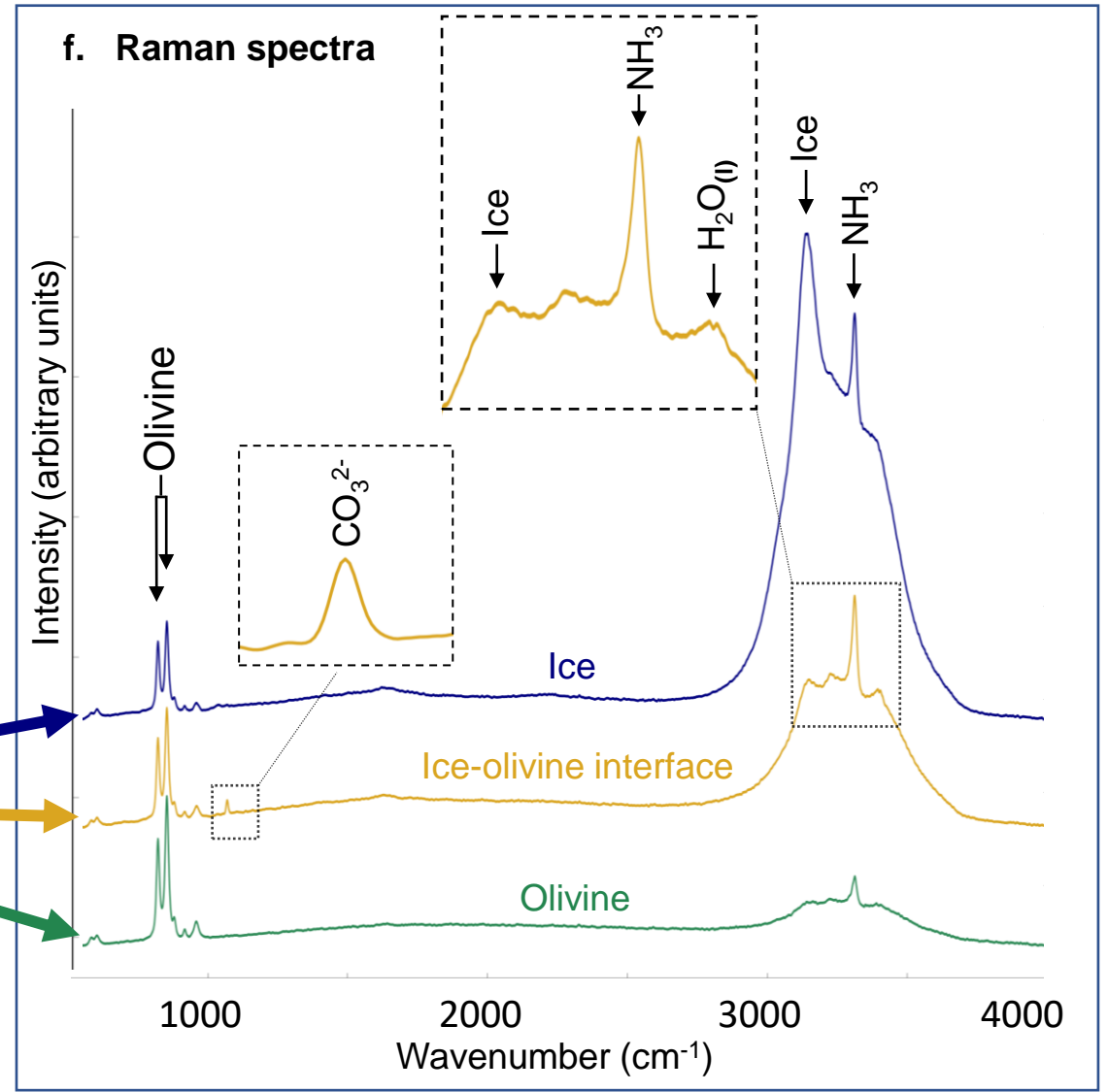
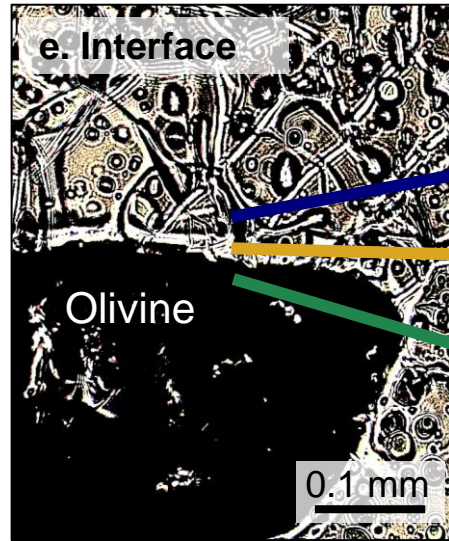
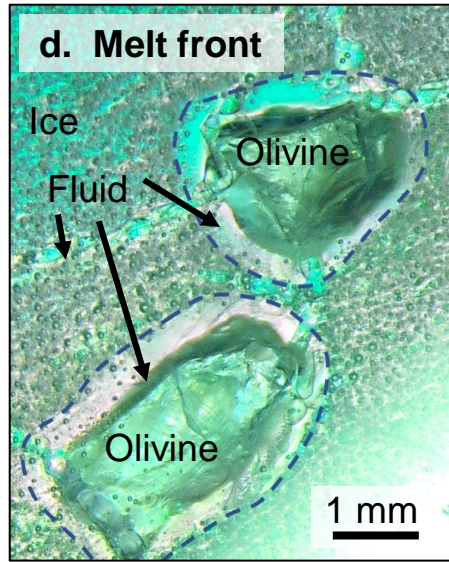
431

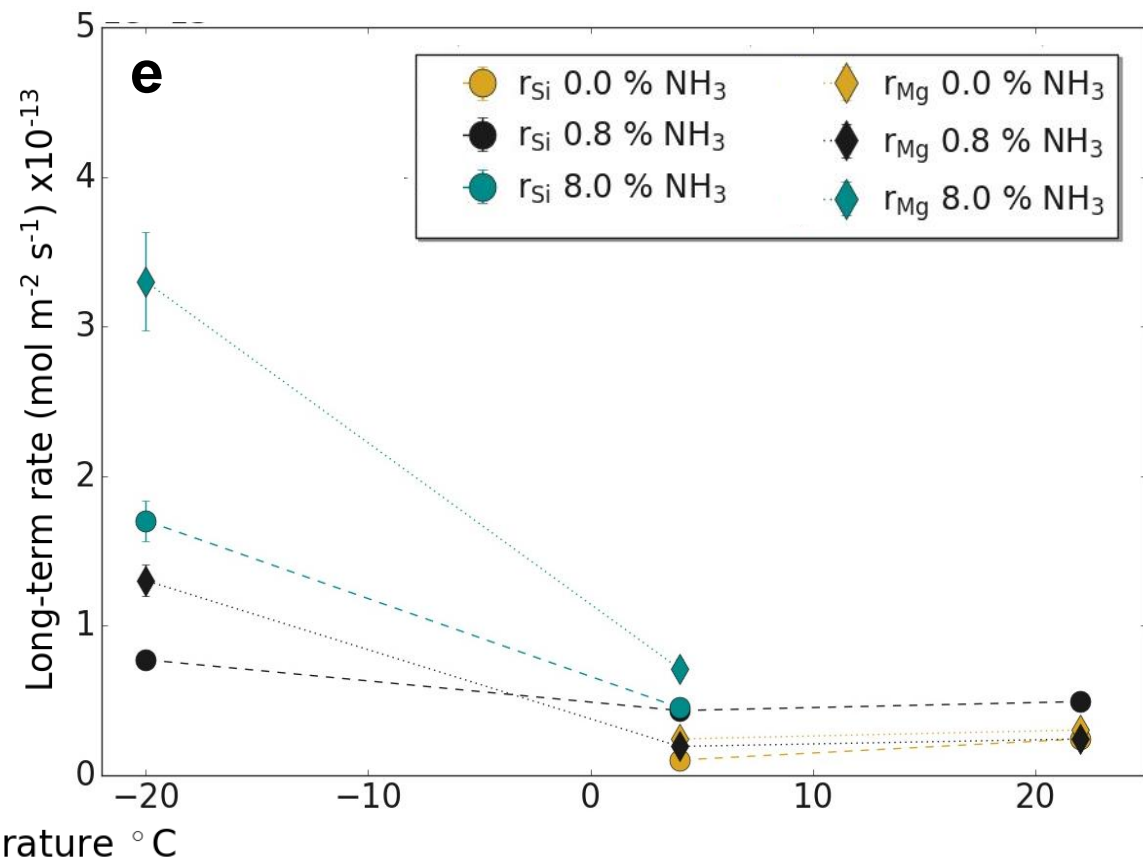
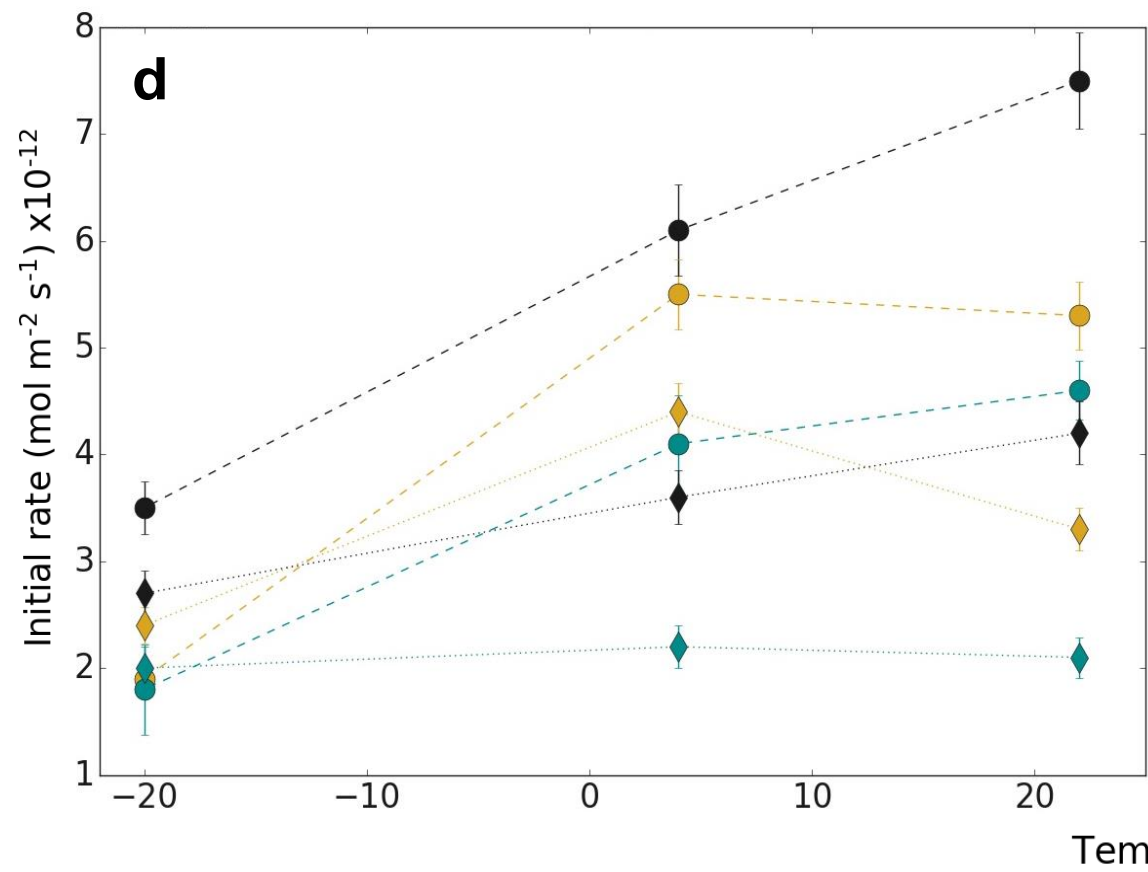
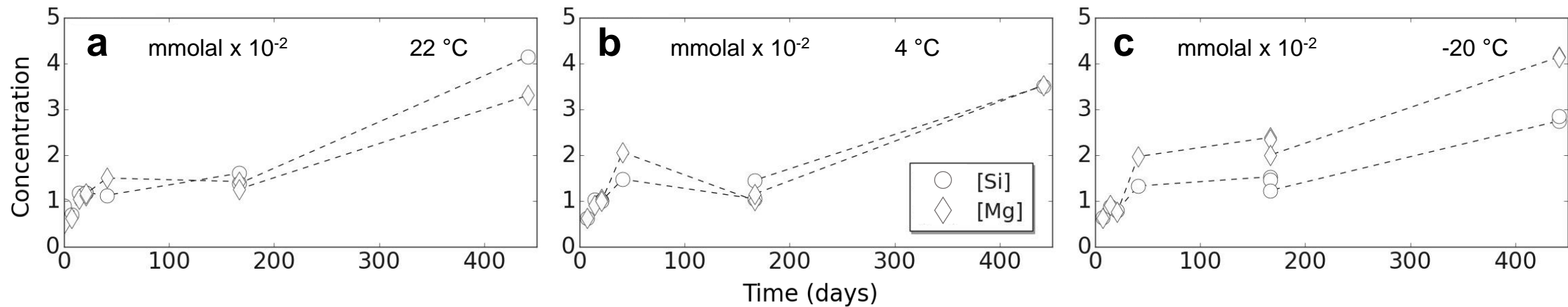
432

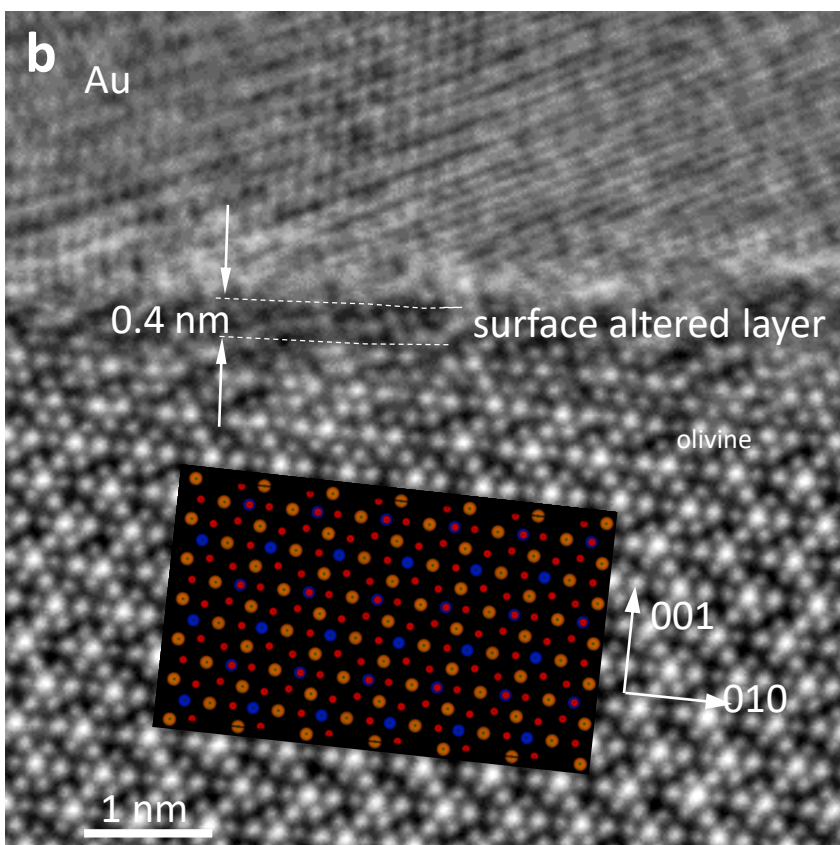
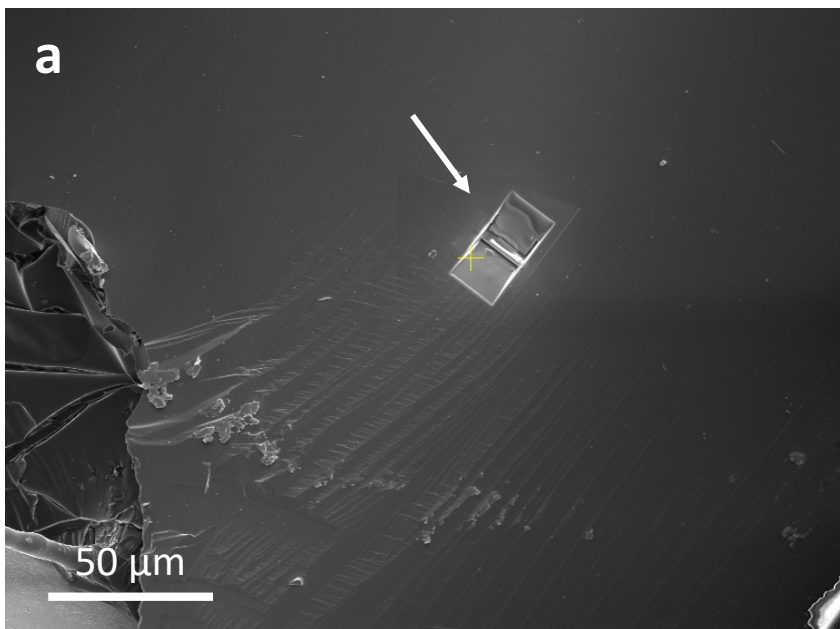
Increasing ice crystallinity / Decreasing  $\text{NH}_3$  content



Fluid at the ice-olivine interface







● Si ● O ● Fe/Mg